2001

X-Ray Standing-Wave Investigations of Valence Electronic Structure

J. C. Woicik

E. J. Nelson

See next page for additional authors

Citation/Publisher Attribution

Woicik, J. C., E. J. Nelson, D. Heskett, J. Warner, L. E. Berman, B. A. Karlin, I. A. Vartanyants, M. Z. Hasan, T. Kendelewicz, Z. X. Shen and P. Pianetta. " X-Ray Standing-Wave Investigations of Valence Electronic Structure." *Physical Review B, Condensed Matter and Materials Physics*. 64(12):125115-1 - 125115-15. 15 September 2001.
Available at http://link.aps.org/doi/10.1103/PhysRevB.64.125115.

X-ray standing-wave investigations of valence electronic structure

J. C. Woicik and E. J. Nelson
National Institute of Standards and Technology, Gaithersburg Maryland 20899

D. Heskett and J. Warner
Department of Physics, University of Rhode Island, Kingston Rhode Island 02881

L. E. Berman
National Synchrotron Light Source, Brookhaven National Lab, Upton New York 11973

B. A. Karlin
National Institute of Standards and Technology, Gaithersburg Maryland 20899

I. A. Vartanyants
Department of Physics, University of Illinois, Urbana, Illinois 61801

M. Z. Hasan, T. Kendelewicz, Z. X. Shen, and P. Pianetta
Stanford Synchrotron Radiation Laboratory, Stanford California 94305

(Received 1 February 2001; revised manuscript received 4 June 2001; published 10 September 2001)

We have examined the valence-electron emission from Cu, Ge, GaAs, InP, and NiO single crystals under the condition of strong x-ray Bragg reflection; i.e., in the presence of the spatially modulated x-ray standing-wave interference field that is produced by the superposition of the incident and reflected x-ray beams. These crystals span the entire metallic, covalent, and ionic range of solid-state bonding. It is demonstrated that the valence-electron emission is closely coupled to the atomic cores, even for electron states close to a metallic Fermi edge. Using the bond-orbital approximation, the x-ray standing-wave structure factor for valence-electron emission is derived in terms of the bond polarities and photoionization cross sections of the atoms within the crystalline unit cell and compared to experiment. Additionally, we demonstrated that by exploiting the spatial dependence of the electric-field intensity under Bragg condition, site specific valence electronic structure may be obtained. The technique is demonstrated for GaAs and NiO.

DOI: 10.1103/PhysRevB.64.125115 PACS number(s): 68.49.Uv, 78.70.Ck, 79.20.−m

I. INTRODUCTION

One of the most powerful experimental tools for examining the electronic structure of a solid or film is photoelectron spectroscopy. Due to the conservation of energy between the incident photon and the ejected photoelectron,[1] much direct and important electronic information pertaining to the occupied valence-band density of states has been obtained for many materials, and this information has been used to establish the validity of complicated band-structure calculations for metals, semiconductors, insulators, and alloys.[2]

Typical photoemission measurements are performed with excitation sources that are monochromatic plane waves. Because the intensity of a plane wave is constant over the dimensions of the crystalline unit cell, standard photoemission measurements are unable to produce direct, site specific valence information. As many of the recent density of states calculations that have been performed for compound materials are element or site specific, such information is necessary for the detailed comparisons between theory and experiment that are necessary to advance our knowledge of solid-state bonding. This limitation of the photoemission technique has been partially mitigated by experiments that have exploited either the photon-energy dependence or Cooper minimum[3] of the atomic cross sections of the atoms within the unit cell[4–6] or the photon-energy dependence or Fano[7] resonant behavior of these atoms near a core-ionization threshold.[8] Additionally, x-ray photoelectron diffraction has also been used to obtain site specific valence information.[9]

In this work, we utilize the spatial dependence of the x-ray standing-wave (XSW) interference field that results from the coherent superposition of the incident and reflected x-ray beams near a crystal x-ray Bragg reflection to examine the valence-electronic structure of a number of materials that span the entire range of solid-state bonding; i.e., metallic, covalent, and ionic. By combining this form of x-ray diffraction with valence-photoelectron spectroscopy, we are able to gain a better experimental understanding of the fundamental physics of the photoemission process. In addition, by selectively positioning the maximum of the electric-field intensity within the crystalline unit cell and recording high-resolution valence-photoelectron spectra, site-specific information on the occupied valence-band density of states may be directly obtained.

II. THEORY OF VALENCE-ELECTRON EMISSION IN AN X-RAY STANDING-WAVE FIELD

We turn our attention to the problem of the photoelectron emission from a valence band of a single crystal. Because the

valence electrons are delocalized, we must consider the emission from all of the atoms within the crystalline-unit cell, rather than from a single type of atom as is typically assumed for standard x-ray standing-wave analysis.[10] Furthermore, we assume that we do not energy discriminate between valence states of different energy. This situation will be discussed in later sections. For simplicity, we assume that our unit cell has two atoms, and we label these atoms as a for the anion sites and c for the cation sites, respectively.

The initial bound-state wave function of a valence electron can be taken in the tight-binding, bond-orbital approximation[11,12] as the sum of the hybridized valence atomic orbitals on each of the cores. As a Bloch wave, our initial-state wave function may therefore be written

$$|i\rangle = \sum_{\mathbf{R}} e^{i\mathbf{k}\cdot\mathbf{R}}[u_a\phi_a(\mathbf{r}-\mathbf{r}_a-\mathbf{R}) + u_c\phi_c(\mathbf{r}-\mathbf{r}_c-\mathbf{R})]. \quad (1)$$

Here $\phi_a(\mathbf{r})$ and $\phi_c(\mathbf{r})$ are the hybrid, atomic-state valence orbitals of atom a and atom c. (For the III-V semiconductors they are the s-p states.) Coefficients u_a and u_c are defined in terms of the bond polarity α_p which is calculated from the Hartree-Fock term values of the free atoms[11]

$$u_a = [(1+\alpha_p)/2]^{1/2} \text{ and } u_c = [(1-\alpha_p)/2]^{1/2}. \quad (2)$$

The coordinate vectors $\mathbf{R}$ describe the positions of the unit cells, and $\mathbf{r}_a$ and $\mathbf{r}_c$ are the positions of the anion and the cation atoms within each unit cell. [For the (111) reflection of the group III-V semiconductors, $\mathbf{r}_c - \mathbf{r}_a = \frac{1}{4}a[111]$, where a is the lattice parameter.]

Since we are working at several keV photon energy, we may use the Born approximation[13] that describes the final-state wave function of the escaping photoelectron as an energetic plane wave travelling with wave vector $\mathbf{k}_f$

$$|f\rangle = e^{i\mathbf{k}_f\cdot\mathbf{r}}. \quad (3)$$

Under the condition of x-ray Bragg reflection, the electric field is given by the superposition of the coherently coupled incident $\mathbf{E}_o$ and reflected $\mathbf{E}_h$ monochromatic plane waves that travel with wave vectors $\mathbf{k}_o$ and $\mathbf{k}_h$, polarization vectors $\mathbf{e}_o$ and $\mathbf{e}_h$, and frequency ω

$$\mathbf{E}(\mathbf{r},t) = [\mathbf{e}_o E_o e^{i\mathbf{k}_o\cdot\mathbf{r}} + \mathbf{e}_h E_h e^{i\mathbf{k}_h\cdot\mathbf{r}}]e^{-i\omega t}. \quad (4)$$

$\mathbf{k}_o$ and $\mathbf{k}_h$ are connected by the Bragg condition $\mathbf{h} = \mathbf{k}_h - \mathbf{k}_o$, where $\mathbf{h}$ is a reciprocal-lattice vector of the crystal.

This field squares to give the wavefield intensity at an arbitrary point $\mathbf{r}$ in space

$$I(\mathbf{r}) = |E_o|^2[1 + R + 2C\sqrt{R}\cos(\nu + \mathbf{h}\cdot\mathbf{r})], \quad (5)$$

where ν is the phase of the complex-field amplitude ratio $E_h/E_o = \sqrt{R}e^{i\nu}$, R is the reflectivity function $R = |E_h/E_o|^2$, and $C = \mathbf{e}_o\cdot\mathbf{e}_h$ is the polarization coefficient which is equal to 1 for σ-polarization and equal to $\cos 2\theta_B$ for π polarization. (θ_B is the Bragg angle.) Both R and ν are functions of photon energy and angle around the Bragg condition. For the symmetric reflections studied in this work $C = 1$, although we will consider both situations in the following derivation.

The general importance of Eq. (5) arises because within the region of dynamical x-ray Bragg diffraction,[14] the phase ν may be continuously varied from 0 to π. Consequently, the maxima (or minima) of the sinusoidal electric-field intensity may be experimentally scanned across the atomic planes of a crystal simply by slightly varying either the angle of the sample or the photon energy around the Bragg condition.

To calculate the cross section of the photoelectron effect in the presence of the x-ray standing-wave field, we must first calculate the differential cross section using the total electric field from Eq. (4). The intensity of the photoexcitation process is proportional to the square modulus of the transition-matrix element M_{if} between the initial and final states[13]

$$d\sigma/d\Omega \propto |M_{if}|^2, \quad (6)$$

where

$$M_{if} = \langle f|E_o e^{i\mathbf{k}_o\cdot\mathbf{r}}(\mathbf{e}_o\cdot\mathbf{p}) + E_h e^{i\mathbf{k}_h\cdot\mathbf{r}}(\mathbf{e}_h\cdot\mathbf{p})|i\rangle, \quad (7)$$

and $\mathbf{p} = -ih\nabla$ is the momentum operator. It follows from Eq. (7) that the matrix element of the photoelectron process is the sum of the matrix elements corresponding to the direct and diffracted waves

$$M_{if} = E_o\langle f|e^{i\mathbf{k}_o\cdot\mathbf{r}}(\mathbf{e}_o\cdot\mathbf{p})|i\rangle + E_h\langle f|e^{i\mathbf{k}_h\cdot\mathbf{r}}(\mathbf{e}_h\cdot\mathbf{p})|i\rangle, \quad (8)$$

or

$$M_{if} = E_o M_{if}(\mathbf{k}_o) + E_h M_{if}(\mathbf{k}_h). \quad (9)$$

We will now calculate each matrix element separately. Using Eqs. (1) and (3) for our initial- and final-state wave functions, and performing the change of variables to electron coordinates $\mathbf{r}_e^a = \mathbf{r} - \mathbf{r}_a - \mathbf{R}$ and $\mathbf{r}_e^c = \mathbf{r} - \mathbf{r}_c - \mathbf{R}$ in each anion and cation term, we arrive at an expression for $M_{if}(\mathbf{k}_o)$

$$M_{if}(\mathbf{k}_o) = \sum_{\mathbf{R}} e^{i(\mathbf{k}+\mathbf{k}_o-\mathbf{k}_f)\cdot\mathbf{R}}[u_a e^{i(\mathbf{k}_o-\mathbf{k}_f)\cdot\mathbf{r}_a} \times \langle f|e^{i\mathbf{k}_o\cdot\mathbf{r}_e^a}(\mathbf{e}_o\cdot\mathbf{p})|\phi_a\rangle + u_c e^{i(\mathbf{k}_o-\mathbf{k}_f)\mathbf{r}_c}\langle f|e^{i\mathbf{k}_o\cdot\mathbf{r}_e^c}(\mathbf{e}_o\cdot\mathbf{p})|\phi_c\rangle]. \quad (10)$$

Performing the sum in Eq. (10) over the coordinates $\mathbf{R}$ of the unit cells, we obtain the conservation law of quasimomentum for the photoelectron process $\Sigma_{\mathbf{R}} e^{i(\mathbf{k}+\mathbf{k}_o-\mathbf{k}_f)\cdot\mathbf{R}} = N\delta_{\mathbf{k}_f,\mathbf{k}+\mathbf{k}_o+\mathbf{g}}$, where N is the number of unit cells, δ is the Kronecker delta, and $\mathbf{g}$ is a reciprocal-lattice vector.[12] Finally, we obtain an expression for the matrix element $M_{if}(\mathbf{k}_o)$

$$M_{if}(\mathbf{k}_o) \propto [u_a e^{i(\mathbf{k}_o-\mathbf{k}_f)\cdot\mathbf{r}_a}V_a(\mathbf{k}_o) + u_c e^{i(\mathbf{k}_o-\mathbf{k}_f)\cdot\mathbf{r}_c}V_c(\mathbf{k}_o)], \quad (11)$$

where the matrix elements $V_a(\mathbf{k}_o)$ and $V_c(\mathbf{k}_o)$

$$V_a(\mathbf{k}_o) = \langle f|e^{i\mathbf{k}_o\cdot\mathbf{r}_e^a}(\mathbf{e}_o\cdot\mathbf{p})|\phi_a,$$

$$V_c(\mathbf{k}_o) = \langle f|e^{i\mathbf{k}_o\cdot\mathbf{r}_e^c}(\mathbf{e}_o\cdot\mathbf{p})|\phi_c\rangle, \quad (12)$$

correspond to the elementary photoexcitation process from the anion and cation sites a and c for the incident beam.

Integration in Eq. (12) is performed over the electron coordinates $\mathbf{r}_e^a$ and $\mathbf{r}_e^c$ which are the electron-position vectors from the anion and cation sites in each integral, respectively.

Performing the same calculation for the diffracted beam, we obtain for the matrix element $M_{if}(\mathbf{k}_h)$

$$M_{if}(\mathbf{k}_h) \propto [u_a e^{i(\mathbf{k}_h-\mathbf{k}_f)\cdot \mathbf{r}_a} V_a(\mathbf{k}_h) + u_c e^{i(\mathbf{k}_h-\mathbf{k}_f)\mathbf{r}_c} V_c(\mathbf{k}_h)], \tag{13}$$

where we also have

$$V_a(\mathbf{k}_h) = \langle f | e^{i\mathbf{k}_h\cdot \mathbf{r}_e^a} (\mathbf{e}_h\cdot\mathbf{p}) | \phi_a \rangle,$$

$$V_c(\mathbf{k}_h) = \langle f | e^{i\mathbf{k}_h\cdot \mathbf{r}_e^c} (\mathbf{e}_h\cdot\mathbf{p}) | \phi_c \rangle. \tag{14}$$

If we now substitute the expressions for the matrix elements of the incident [Eq. (11)] and diffracted [Eq. (13)] beams into Eq. (9), after some algebra we arrive at the most general expression for the transition-matrix element for the photoelectron effect from a crystal-valence band

$$\begin{aligned} M_{if} = E_o \{ & u_a e^{i(\mathbf{k}_o-\mathbf{k}_f)\cdot\mathbf{r}_a} [V_a(\mathbf{k}_o) + (E_h/E_o) e^{i\mathbf{h}\cdot\mathbf{r}_a} V_a(\mathbf{k}_h)] \\ & + u_c e^{i(\mathbf{k}_o-\mathbf{k}_f)\cdot\mathbf{r}_c} [V_c(\mathbf{k}_o) + (E_h/E_o) e^{i\mathbf{h}\cdot\mathbf{r}_c} V_c(\mathbf{k}_h)] \}. \end{aligned} \tag{15}$$

From Eq. (6), taking the magnitude squared of this expression gives us the differential cross section for the valence-electron emission in the presence of two coherently coupled x-ray beams

$$\begin{aligned} d\sigma/d\Omega \propto & u_a^2 |V_a(\mathbf{k}_o) + (E_h/E_o) e^{i\mathbf{h}\cdot\mathbf{r}_a} V_a(\mathbf{k}_h)|^2 \\ & + u_c^2 |V_c(\mathbf{k}_o) + (E_h/E_o) e^{i\mathbf{h}\cdot\mathbf{r}_c} V_c(\mathbf{k}_h)|^2 \\ & + u_a u_c e^{i(\mathbf{k}_o-\mathbf{k}_f)\cdot(\mathbf{r}_c-\mathbf{r}_a)} [V_a(\mathbf{k}_o) \\ & + (E_h/E_o) e^{i\mathbf{h}\cdot\mathbf{r}_a} V_a(\mathbf{k}_h)]^* \\ & \times [V_c(\mathbf{k}_o) + (E_h/E_o) e^{i\mathbf{h}\cdot\mathbf{r}_c} V_c(\mathbf{k}_h)] + \text{c.c.} \end{aligned} \tag{16}$$

Note that the equation usually used to study x-ray photoelectron emission from a crystal-valence band from one propagating electromagnetic beam[4,15] is obtained from Eq. (16) by setting $E_h = 0$.

As we are interested in the integral photoeffect, we will be integrating Eq. (16) over all solid angle $d\Omega$. As valence electrons have negligible binding energies ($\varepsilon_b \sim 0$), the product $|(\mathbf{k}_o-\mathbf{k}_f)\cdot(\mathbf{r}_c-\mathbf{r}_a)|$ will be much greater than 1 at x-ray energies; consequently, the phase factor $e^{i(\mathbf{k}_o-\mathbf{k}_f)\cdot(\mathbf{r}_c-\mathbf{r}_a}$ will be highly oscillatory, and therefore the cross terms can be neglected compared to the first two terms of Eq. (16).[4,15,16] This approximation leads us to the differential cross section for two independent, mixed-site emitters in the presence of two coherently coupled x-ray beams

$$\begin{aligned} d\sigma/d\Omega \propto & u_a^2 |V_a(\mathbf{k}_o) + (E_h/E_o) e^{i\mathbf{h}\cdot\mathbf{r}_a} V_a(\mathbf{k}_h)|^2 \\ & + u_c^2 |V_c(\mathbf{k}_o) + (E_h/E_o) e^{i\mathbf{h}\cdot\mathbf{r}_c} V_c(\mathbf{k}_h)|^2. \end{aligned} \tag{17}$$

For the moment, we will make the dipole approximation[13] in the matrix elements of Eqs. (12) and (14) that $e^{i\mathbf{k}_o\cdot\mathbf{r}_e^{a,c}} \sim e^{i\mathbf{k}_h\cdot\mathbf{r}_e^{a,c}} \sim 1$. Due to the spatial extent of the valence electrons, one might not expect the dipole approximation to be valid. However, again because a valence electron has negligible binding energy, it becomes a good approximation for the low x-ray energies that the momentum of the photon may be neglected compared to the momentum of the electron inside the matrix elements; i.e., $k_f \gg k_{o,h}$.[13] Additionally, because we are utilizing a bond-orbital wave function, the dipole approximation is implicit because ϕ_a and ϕ_c are atomic orbitals. (We will address higher-order multipole terms shortly.) Consequently, because the directions of propagation of the incident and diffracted x-ray beams do not affect the matrix elements, all the terms in Eq. (17) are directly proportional to the total cross sections of the anion and cation wave functions within this approximation

$$\begin{aligned} & \int |V_a(\mathbf{k}_{o,h})|^2 d\Omega \propto \sigma_a^T, \\ & \int |V_c(\mathbf{k}_{o,h})|^2 d\Omega \propto \sigma_c^T, \\ & \int V_a^*(\mathbf{k}_o) V_a(\mathbf{k}_h) d\Omega \propto C\sigma_a^T, \\ & \int V_c^*(\mathbf{k}_o) V_c(\mathbf{k}_h) d\Omega \propto C\sigma_c^T. \end{aligned} \tag{18}$$

From Eqs. (17) and (18), we now obtain the intensity of the total valence-electron emission from the two coherently coupled beams

$$\begin{aligned} Y_T = & u_a^2\sigma_a^T [1 + R + 2C\sqrt{R}\cos(\nu + \mathbf{h}\cdot\mathbf{r}_a)] \\ & + u_c^2\sigma_c^T [1 + R + 2C\sqrt{R}\cos(\nu + \mathbf{h}\cdot\mathbf{r}_c)]. \end{aligned} \tag{19}$$

Comparison with Eq. (5) shows that the valence-electron emission associated with each atom is directly proportional to the electric-field intensity at the location of its electronic core.

The above expression can be written in the usual parametrized form of the XSW yield from an ensemble of atoms[10]

$$Y_T = 1 + R + 2C\sqrt{R}F\cos(\nu - 2\pi D), \tag{20}$$

where the parameters D and F are referred to as the coherent position and coherent fraction, respectively. (For core-emission XSW measurements, D and F may be interpreted as the phase and amplitude of the charge-density Fourier coefficient for the $\mathbf{h}$ reflection.[17])

Using a trigonometric identity, Eqs. (19) and (20) render

$$Fe^{i2\pi D} = [u_a^2\sigma_a^T e^{i\mathbf{h}\cdot\mathbf{r}_a} + u_c^2\sigma_c^T e^{i\mathbf{h}\cdot\mathbf{r}_c}]/[u_a^2\sigma_a^T + u_c^2\sigma_c^T], \tag{21}$$

which may be generalized for a unit cell with an arbitrary number of i atoms

$$Fe^{i2\pi D} = \sum_i u_i^2\sigma_i^T e^{i\mathbf{h}\cdot\mathbf{r}_i} \Big/ \sum_i u_i^2\sigma_i^T. \tag{22}$$

Equation (22) is the x-*ray standing-wave structure factor for valence-electron emission*. Note that both the bond polarities and photoelectron cross sections appear in Eq. (22).

It is also possible to take into account nondipole contributions to the x-ray standing-wave yield. This amounts to including the first term in the Taylor-series expansion of the retardation terms in Eq. (18); i.e., $e^{i\mathbf{k}_o\cdot\mathbf{r}_e{}^{a,c}}\sim 1+i\mathbf{k}_o\cdot\mathbf{r}_e^{a,c}$ and $e^{i\mathbf{k}_h\cdot\mathbf{r}_e{}^{a,c}}\sim 1+i\mathbf{k}_h\cdot\mathbf{r}_e^{a,c}$. According to the results of Ref. [18], we may write the integrals of Eq. (18) in terms of their dipole and quadrupole contributions

$$\int |V_a(\mathbf{k}_{o,h})|^2 d\Omega \propto \sigma_a^D+\sigma_a^Q,$$

$$\int |V_c(\mathbf{k}_{o,h})|^2 d\Omega \propto \sigma_c^D+\sigma_c^Q,$$

$$\int V_a^*(\mathbf{k}_o)V_a(\mathbf{k}_h)d\Omega \propto C^D\sigma_a^D+C^Q\sigma_a^Q,$$

$$\int V_c^*(\mathbf{k}_o)V_c(\mathbf{k}_h)d\Omega \propto C^D\sigma_c^D+C^Q\sigma_c^Q, \qquad (23)$$

where $\sigma_{a,c}^D$ and $\sigma_{a,c}^Q$ are the total dipole and quadrupole cross sections for the anion and cation atoms, and $C^D=\mathbf{e}_o\cdot\mathbf{e}_h$ and $C^Q=[(\mathbf{e}_o\cdot\mathbf{e}_h)(\mathbf{k}_o\cdot\mathbf{k}_h)+(\mathbf{e}_o\cdot\mathbf{k}_h)(\mathbf{e}_h\cdot\mathbf{k}_o)]/|\mathbf{k}_o|^2$ are the dipole and quadrupole polarization parameters. Equation (19) is then modified to include the ratio of the dipole to quadrupole cross sections for the angle-integrated yield

$$Y_T=u_a^2\sigma_a^T[1+R+2C^D(1-Q_a)\sqrt{R}\cos(\nu+\mathbf{h}\cdot\mathbf{r}_a)] + u_c^2\sigma_c^T[1+R+2C^D(1-Q_c)\sqrt{R}\cos(\nu+\mathbf{h}\cdot\mathbf{r}_c)]. \qquad (24)$$

where $\sigma_{a,c}^T=\sigma_{a,c}^D+\sigma_{a,c}^Q$, polarization coefficient $C^D=1$ for σ polarization and $C^D=\cos 2\theta_B$ for π polarization, and $Q_{a,c}$ are the quadrupole contributions for the anion and cation sites, respectively. They are equal to

$$Q_{a,c}=2(\sigma^Q/\sigma^T)_{a,c}\sin^2\theta_B \qquad (25)$$

for σ polarization and

$$Q_{a,c}=2(\sigma^Q/\sigma^T)_{a,c}[\cos 2\theta_B-\cos 4\theta_B]/\cos 2\theta_B. \qquad (26)$$

for π polarization. Note that the inclusion of the quadrupole contributions to the integral photoyield breaks the strict proportionality between the electric-field intensities and the valence-electron emissions found in Eq. (19) by reducing the amplitudes or coherent fractions of the x-ray standing-wave modulations. The coherent position will also be affected, but only in cases where Q_a and Q_c are large and differ by a significant amount.

III. EXPERIMENTAL DETAILS

The experimental studies of the covalent semiconductors Ge, GaAs, and InP were performed at the Stanford Synchrotron Radiation Laboratory using the ''Jumbo'' double-crystal monochromator and a standard ultra-high vacuum chamber. Electron-emission, back-reflection x-ray standing-wave data[10,19,20,21] were recorded in a fixed-angle, normal-incidence diffraction geometry by scanning the monochromator and a double-pass cylindrical-mirror analyzer (CMA) simultaneously through the photon-energy range of the crystal x-ray Bragg back reflection. The CMA was operated with x-ray photoelectron-spectroscopy slits and a pass energy of 200 eV to give an electron-energy resolution of ~3.2 eV. The horizontal axis of the spectrometer was aligned parallel to the polarization vector of the synchrotron radiation, and a pair of InSb(111) crystals provided the monochromatized x-ray beam. In this geometry, the CMA accepts electrons with an angular range of ~6° about the CMA cone which has a half angle of 42.3° with respect to the CMA axis. Fiducial information on the photon energy, the photon-energy rocking-curve width (~0.7 eV), and the sample alignment was obtained from the reflectivity curves which were measured simultaneously to the electron-emission curves with an I_o grid upstream of the sample.

(111) back-reflection x-ray standing-wave data were recorded from freshly cleaved Ge(111). From freshly cleaved GaAs(110), GaAs(-1-10), InP(110), and InP(−1−10), (111), (−1−1−1), (111), and (−1−1−1) back-reflection x-ray standing-wave data were recorded, respectively. The sample geometries were adjusted to make the incident beam normal to either the (111) or (−1−1−1) diffraction planes. Ge $3d$, Ga $3d$, As $3d$, In $4d$, and P $2s$ core-level intensity data were recorded in addition to the intensity from the top of each crystal-valence band as the photon energy was scanned through the Bragg back-reflection condition. Only in the case of the P $2s$ core line was it necessary to measure the modulation of the inelastic-electron background at a slightly higher kinetic energy and then subtract it from the data recorded at the kinetic energy of the elastic core line. (The valence band has no extrinsic inelastic background due to electron emission at higher kinetic energies, and the signal to background is large for the other core levels.)

We also examined the core- and valence-photoelectron spectra at fixed photon energies for the GaAs(111) and GaAs(−1−1−1) reflections with the CMA operating with a pass energy of 50 eV, to give a high-resolution electron-energy width of ~0.8 eV. For the GaAs(111) reflection, these data were recorded with the photon energy set to place the maximum of the electric-field intensity near the Ga atomic planes, and for the GaAs(−1−1−1) reflection, these data were recorded with the photon energy set to place the maximum of the electric-field intensity near the As atomic planes.

The experimental studies of Cu and NiO were conducted at the National Synchrotron Light Source using beamline *X24a* and a standard ultra-high vacuum chamber. This double-crystal monochromator was operated with Si(111) crystals, and electron-emission spectra were recorded with a multichannel hemispherical analyzer. Atomically clean Cu surfaces were produced by repeated cycles of argon sputtering and annealing. NiO surfaces were produced by repeated cycles of argon sputtering and annealing in oxygen.[22] For the x-ray standing-wave experiments, the Cu(111) crystal was aligned so that the (11−1) diffracting planes were normal to the synchrotron beam, and the NiO(001) crystal was aligned so that the (111) diffracting planes were normal to the synchrotron beam. For both the Cu and NiO studies, the horizontal axis of the spectrometer was aligned parallel to the

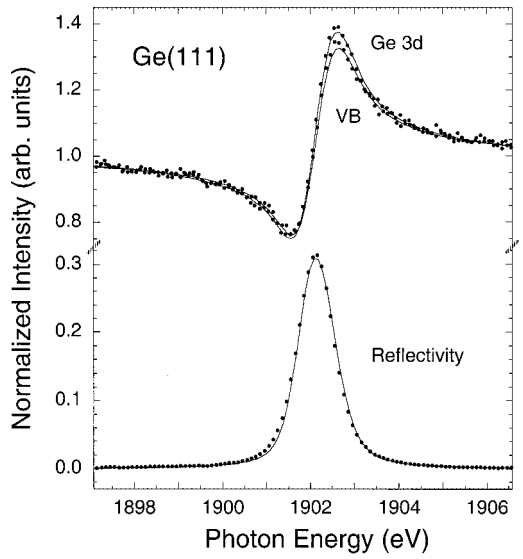

FIG. 1. Photon-energy dependence of the Ge 3*d* and the Ge valence-electron emission near the Ge(111) Bragg back-reflection condition. Also shown is the Ge(111) reflectivity curve. The lines are the theoretical fits to the data points.

polarization vector of the synchrotron radiation. In this geometry, the hemispherical analyzer accepts electrons within a cone of $\pm 20°$ with respect to the polarization vector.

Unlike the CMA, the hemispherical analyzer utilizes a multichannel detector plate, so Cu x-ray standing-wave electron-emission data were recorded by setting an analyzer window around either the Cu $3p$ core line or the Cu valence band and summing the counts in all of the 16 channels of the analyzer while a bias voltage connected to the sample was scanned together with the photon energy. Cu and NiO photoelectron spectra were collected at different photon energies around the Bragg condition by setting the photon energy and scanning the electron analyzer in a high-resolution mode. For the Cu data, valence spectra were recorded with a pass energy of 11.75 eV to give an electron-energy resolution of $\sim$0.18 eV. For NiO, a pass energy of 23.50 eV was used to give an electron-energy resolution of $\sim$0.35 eV. In both cases, the photon-energy width was $\sim$0.45 eV.

IV. RESULTS

A. Covalent semiconductors

1. Homopolar Ge

Figure 1 compares the photon-energy dependence of the Ge 3*d* core-level emission with the Ge valence-electron emission in the vicinity of the Ge(111) Bragg back-reflection condition. These are raw electron-yield curves recorded by scanning both the monochromator and CMA simultaneously; they have been scaled only by a constant to make equal their yield away from the energy of the crystal Bragg back reflection. Additionally, they have been recorded in quick, alternating scan-by-scan succession by changing only the detection energy of the CMA in order to eliminate any systematic

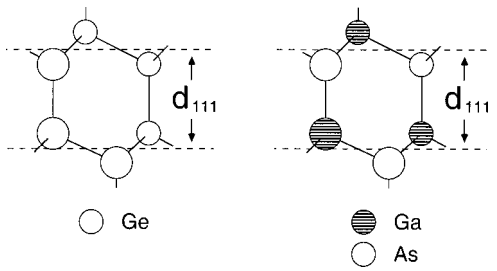

FIG. 2. Side views of the Ge(111) and GaAs(111) crystal structures. The (111) atomic planes are indicated.

errors between them. The lower part of the figure shows the reflectivity curve recorded simultaneously with the electron-emission data.

The Ge 3*d* core-level emission shows the characteristic x-ray standing-wave pattern from this centrosymmetric crystal.[23] The emission from the delocalized valence band is startlingly similar, showing only a small reduction in XSW amplitude.

In order to obtain quantitative information, following standard XSW analysis, these data were fit by Eq. (20) ($C=1$), using the photon-energy offset and photon-energy width obtained from the fit to the reflectivity data. The complex-reflectivity function was calculated from the dynamical theory of x-ray diffraction;[14] both R and ν are functions of photon energy. The pertinent XSW fitting parameters are D, the average position of the resulting emission relative to the diffracting planes in units of the reflecting plane spacing, and F, the coherent fraction of emission that arises from D.

For the Ge 3*d* core distribution, D and F are found to be $D=+0.019\pm0.009$ and $F=+0.682\pm0.038$.[24] These parameters are indistinguishable from the expected values of $D=0$ and $F=0.71$ for the ideal, nonvibrating[25] lattice sites shown in Fig. 2. Note that for this centrosymmetric reflection, the (111) atomic planes bisect the Ge(111) double layer; consequently, F is not equal to 1, but rather it is equal to $\cos(\pi/4)=\sqrt{2}/2=0.71$. This reduction in amplitude reflects the spread of positions between the two spectroscopically indistinguishable Ge atoms of the diamond-unit cell, which are displaced by a quarter of a (111) lattice constant along the [111] direction. [The two Ge atoms of the unit cell have displacements of $+\frac{1}{8}$ and $-\frac{1}{8}$ (111) lattice spacings from the center of the (111) diffraction planes.] For the valence distribution, the same fitting procedure finds $D=0.002\pm0.011$ and $F=0.650\pm0.045$.

2. Heteropolar GaAs and InP

Figure 3 compares the photon-energy dependence of the Ga 3*d*, the As 3*d*, and the GaAs valence-electron emission in the vicinity of the GaAs(111) Bragg back-reflection condition. For the GaAs(111) reflection, the Ga atoms occupy the top half of the diamond bilayer, and the As atoms occupy the bottom half, as shown in Fig. 2. This is easily verified experimentally by the Ga 3*d* and the As 3*d* core-level XSW-emission patterns that show the characteristic yield for each site.[23] Unlike the case of the centrosymmetric Ge planes,

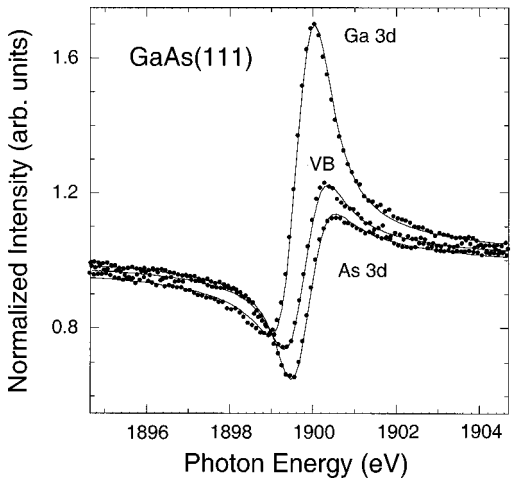

FIG. 3. Photon-energy dependence of the Ga $3d$, the As $3d$, and the GaAs valence-electron emission near the GaAs(111) Bragg back-reflection condition. The lines are the theoretical fits to the data points.

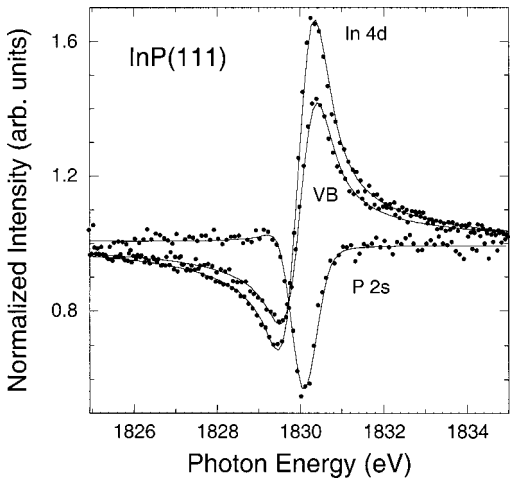

FIG. 5. Photon-energy dependence of the In $4d$, the P $2s$, and the InP valence-electron emission near the InP(111) Bragg back-reflection condition. The lines are the theoretical fits to the data points.

these noncentrosymmetric sites are displaced by $+\frac{1}{8}$ (Ga) and $-\frac{1}{8}$ (As) (111) lattice spacings from the center of the GaAs bilayer, and each of the sites produces a coherent fraction much closer to 1. The valence pattern appears similar to the average of the Ga and As core-level patterns, but it is shifted significantly towards the As site.

To demonstrate that this result is not an experimental artifact, we also collected $(-1-1-1)$ electron-emission data from the same GaAs crystal. These data are shown in Fig. 4. The positions of the Ga and As atoms are now reversed, as seen from the core-level emission patterns. Once again, the valence-emission pattern is close to the average of the two sites, but it is skewed significantly toward the As site.

Figure 5 shows similar data for InP acquired from the InP(111) reflection. Figure 6 shows similar data acquired from the InP$(-1-1-1)$ reflection. We also chose to study InP because, unlike GaAs, the principal quantum numbers of the hybridized valence electrons differ by 2; i.e., the valence band is composed of the hybridized P $3s$ and $3p$ electrons and the In $5s$ and $5p$ electrons. Consequently, atomic cross-section effects should be more apparent in the InP data than in the GaAs data.

An interesting consequence of the large difference in atomic number between the In and P atoms is that the position of the diffracting planes does not coincide with the center of the atomic planes. Rather, the position of the diffracting planes is shifted significantly towards the In sites, as evidenced by the In and P core-level emission patterns. This situation arises due to the large difference in the atomic form factors of In and P that appear in the x-ray structure factor.[26] (The atomic form factors are included in the determination of the atomic positions.) For Ge, the reflection is symmetric. So, in the absence of anomalous dispersion, the Ge charge

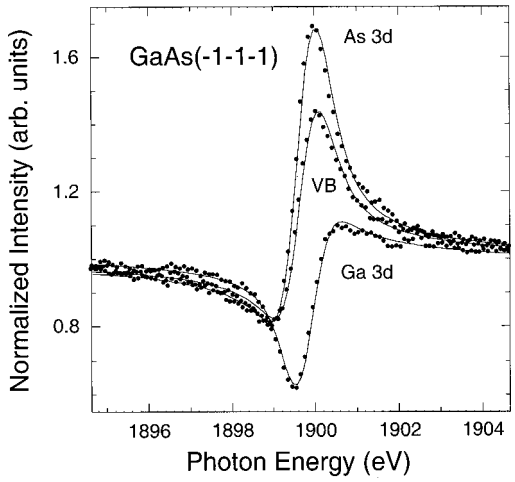

FIG. 4. Photon-energy dependence of the Ga $3d$, the As $3d$, and the GaAs valence-electron emission near the GaAs$(-1-1-1)$ Bragg back-reflection condition. The lines are the theoretical fits to the data points.

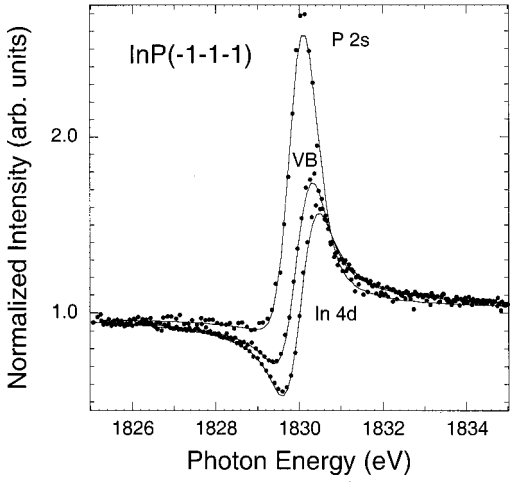

FIG. 6. Photon-energy dependence of the In $4d$, the P $2s$, and the InP valence-electron emission near the InP$(-1-1-1)$ Bragg back-reflection condition. The lines are the theoretical fits to the data points.

TABLE I. XSW fitting parameters D, coherent position, and F, coherent fraction, for the covalent semiconductors Ge, GaAs, and InP.

Ge(111)		
Ge3d	$D=+0.019\pm0.009$	$F=+0.682\pm0.038$
VB	$D=+0.002\pm0.011$	$F=+0.650\pm0.045$
GaAs(111)		
Ga3d	$D=+0.107\pm0.009$	$F=+0.775\pm0.047$
As3d	$D=-0.096\pm0.006$	$F=+0.776\pm0.029$
VB	$D=-0.055\pm0.010$	$F=+0.667\pm0.040$
GaAs($-1\ -1\ -1$)		
Ga3d	$D=-0.100\pm0.011$	$F=+0.827\pm0.053$
As3d	$D=+0.136\pm0.014$	$F=+0.821\pm0.076$
VB	$D=+0.072\pm0.015$	$F=+0.605\pm0.061$
InP(111)		
In4d	$D=+0.111\pm0.010$	$F=+0.811\pm0.049$
P2s	$D=-0.133\pm0.016$	$F=+0.880\pm0.080$
VB	$D=+0.051\pm0.012$	$F=+0.660\pm0.050$
InP($-1\ -1\ -1$)		
In4d	$D=-0.126\pm0.009$	$F=+0.970\pm0.054$
P2s	$D=+0.133\pm0.025$	$F=+1.065\pm0.183$
VB	$D=-0.062\pm0.014$	$F=+0.746\pm0.066$

distribution is uniformly distributed across the diffracting planes; consequently, the position of the diffracting planes and the center of the atomic planes coincide. For GaAs, As has a larger atomic number than Ga; consequently, the diffracting planes are shifted toward the As site, but not by a large amount.[26] For InP, the effect is much greater due to the much larger difference in atomic number.

Table I shows the resulting fitting parameters D and F for the various core levels and the crystal-valence bands of the covalent semiconductors. Note that in the case of the GaAs data, the valence emission is skewed towards the As (anion) sites, whereas for the InP data, the valence emission is skewed towards the In (cation) sites. Clearly, the importance of the atomic cross sections in Eq. (19) is immediately evident because the direction of the charge transfer is the same for both GaAs and InP; i.e., from the positively charged cation to the negatively charged anion.

3. Site-specific valence-electronic structure

We also collected high-resolution valence photoemission spectra at fixed photon energies around the GaAs(111) and the GaAs($-1-1-1$) reflections with the CMA pass energy set at 50 eV. For the (111) reflection, these data were collected with the electric-field intensity maximum placed close to the Ga atomic planes, and for the ($-1-1-1$) reflection, these data were collected with the electric-field intensity maximum placed close to the As atomic planes, as shown in Fig. 7. These experimental geometries and photon energies correspond to the peaks in the Ga and As core-level scanned XSW data of Figs. 3 and 4, respectively. Both reflections were utilized in order to maximize the contrast between the electric-field intensities on the Ga atomic sites and on the As atomic sites.

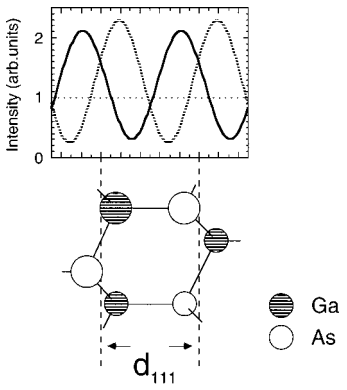

FIG. 7. Theoretical calculations of the normalized electric-field intensity for the GaAs(111) (shaded line) and GaAs($-1-1-1$) (solid line) Bragg back-reflection conditions at photon energy $\hbar\omega = 1900.05$ eV. This photon energy maximizes the electric-field intensity on the Ga atomic planes for the (111) reflection and on the As atomic planes for the ($-1-1-1$) reflection. The spatial positions of the field intensities within the GaAs unit cell are shown relative to the Ga and As atomic planes. The dotted line represents the electric-field intensity away from the Bragg condition which is constant and equal to 1 throughout the unit cell.

Figure 8 shows the resulting GaAs crystal valence-band spectra, referenced to the valence-band maximum. These data are characteristic of the GaAs valence-band density of states.[27,28] The intensities of the three different lobes observed in the spectra modulate significantly depending on which of the atomic planes; i.e., either the anion or cation atomic planes, was preferentially excited. The features at the lowest and highest kinetic energies are enhanced when the

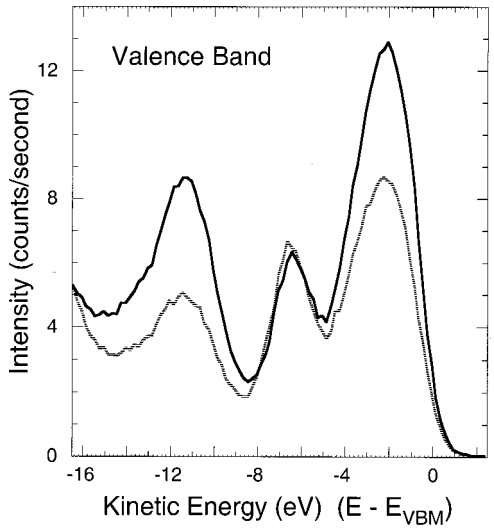

FIG. 8. Comparison of the Ga (shaded line) and As (solid line) on-atom GaAs valence-photoemission spectra. Note the sensitivity of the spectra to the location of the electric-field intensity within the crystalline-unit cell. The features at the lowest and highest binding energies are enhanced when the maximum of the electric-field intensity is placed on the As atomic cores, whereas the feature at intermediate kinetic energy is enhanced when the maximum of the electric-field intensity is placed on the Ga atomic cores.

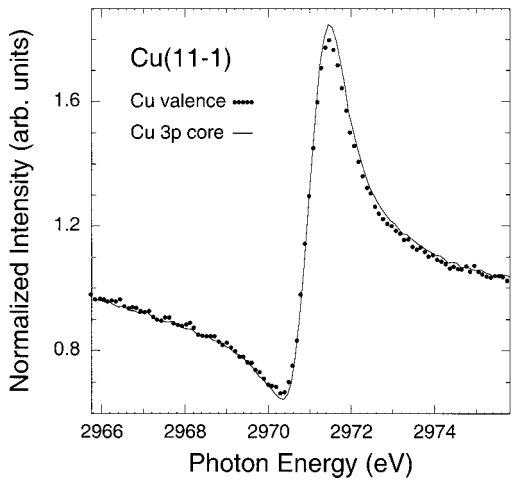

FIG. 9. Photon-energy dependence of the Cu $3p$ core (solid line) and the Cu valence-electron emission (dots) near the Cu(11−1) Bragg back-reflection condition.

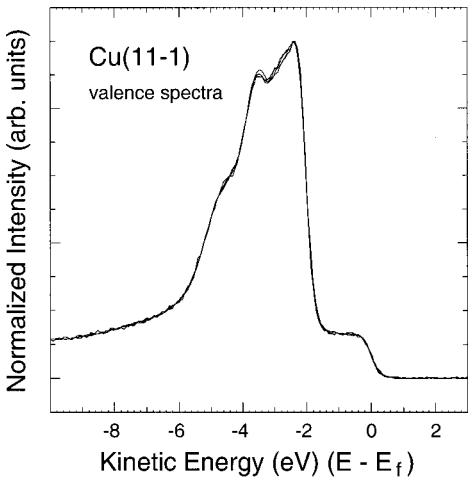

FIG. 10. Comparison of the high-resolution Cu valence-photoemission spectra. The spectra have been normalized to equal peak height and referenced to the Fermi energy. The large peak at intermediate binding energy arises from the Cu $3d$ contribution to the Cu density of states, while the emission near the Fermi energy is of $4s$ origin. The spectral line shapes are indistinguishable within the experimental uncertainties.

maximum of the electric-field intensity is placed on the As atomic sites, whereas the feature at the intermediate kinetic energy is enhanced when the maximum of the electric-field intensity is placed on the Ga atomic sites.

B. Metallic Cu

The XSW emission patterns and high-resolution photoemission spectra from a Cu(111) surface were also studied. Figure 9 compares the photon-energy dependence of the Cu $3p$ core-and valence-electron emission in the vicinity of the Cu(11−1) Bragg back-reflection condition. Once again, these are raw electron-yield curves; they have been scaled only by a constant to make equal their yield away from the Bragg condition. Additionally, they have been recorded in quick, alternating scan-by-scan succession by changing only the detection energy of the analyzer in order to eliminate any systematic errors between them.

As in the case of crystalline Ge, the photon-energy dependence of the valence-electron emission is startlingly similar to the photon-energy dependence of the core-electron emission; the valence-emission pattern shows only a small reduction in XSW amplitude or coherent fraction relative to the core-emission pattern.

These data were also fit by Eq. (20). For the core distribution $D=+0.994\pm0.013$ and $F=+0.918\pm0.069$, while for the valence distribution $D=+0.990\pm0.012$ and $F=+0.870\pm0.061$.

Although the Cu valence band is composed mostly of Cu $3d$ electrons, the less tightly bound electronic states extending to the Fermi edge are composed of the Cu $4s$ electrons.[29] In anticipation of the data presented in Fig. 9, it was our belief that the $4s$ states composing the Fermi edge would be less ''atomiclike'' and therefore more ''free-electron-like'' than the more tightly bound and structured $3d$ states. Consequently, we presumed that the states at the Fermi edge would account for the small reduction in coherence or amplitude of the Cu XSW valence-emission pattern relative to the core-emission pattern observed in Fig. 9.

In order to test this hypothesis, we recorded high-resolution valence-photoelectron spectra at different photon energies throughout the energy width of the Cu(11−1) reflection; i.e., with the electric-field intensity maximum placed on the Cu sites, between the Cu sites in the region of maximum bonding charge, intermediate to these two extremes, and with the photon energy set ~5 eV below the Bragg condition where $R=0$ and the electric-field intensity is constant over the dimensions of the Cu unit cell. These spectra are shown in Fig. 10. They have been referenced to the Fermi level and scaled to equal peak height. The weak region of flat emission near the Fermi level is due to the Cu $4s$ band, and the intense, more tightly bound and structured features are due to the Cu $3d$ emission.

Experimentally, these lineshapes are indistinguishable; therefore, it is clear that the entire Cu valence band or, equivalently, each-energy state of the valence band has the same response to the x-ray standing-wave interference field. We may therefore conclude that all of the Cu valence electrons contribute equally to the experimentally observed small reduction in valence coherent fraction, independent of their initial-state binding energy.

C. Ionic NiO

We also studied the valence-electron emission from the ionic crystal NiO. Unlike the crystal structures studied above that are all formed from the face-centered cubic lattice, NiO crystallizes in the NaCl rocksalt structure.[30] The polar (111) reflections allow the placement of the x-ray standing-wave electric-field intensity maximum on either the Ni or O atomic sites.

Figure 11 shows the x-ray photoelectron spectrum from the spin-orbit split Ni $2p_{1/2}$ and Ni $2p_{3/2}$ core levels. The spin-orbit splitting is ~17.3 eV. In addition to the main spec-

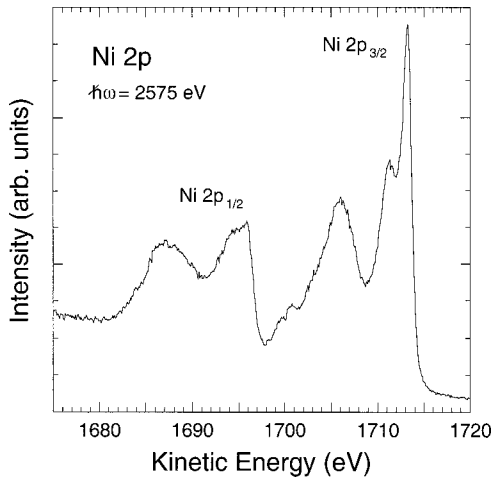

FIG. 11. High resolution Ni $2p$ core-photoemission spectrum from NiO.

tral lines, there are several additional satellite features that are of many-body origin. Similar features are apparently also present in the valence-band spectra which are shown in Fig. 12. The valence spectra were recorded near the NiO(111) Bragg back-reflection condition with the electric-field intensity maximum placed close to the Ni atomic sites and with the electric-field intensity maximum placed close to the O atomic sites. They have been scaled to equal peak height at the top of the Ni $3d$ valence band, which occurs at ~1 eV binding energy. They have also been referenced to the valence-band maximum. The peak at ~20.5 eV binding energy in the valence-band spectra is the O $2s$ line.

Upon comparison of the Ni $2p$ core spectrum with the valence spectra, it is clear that both satellite features occurring at ~1.9 and ~7.3 eV below the main line in the Ni $2p$

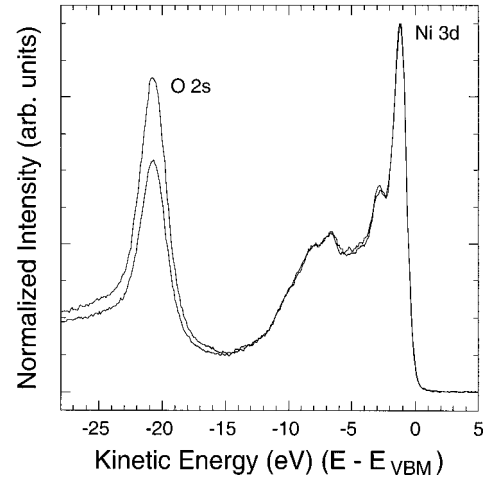

FIG. 12. Comparison of the high-resolution NiO valence-photoemission spectra recorded with the electric-field intensity maximum placed close to the Ni atomic sites and with the electric-field intensity maximum placed close to the O atomic sites. The spectra have been normalized to equal peak height at the top of the Ni $3d$ band and referenced to the valence-band maximum. The spectra are indistinguishable at kinetic energies higher than the O $2s$ level within the experimental uncertainties.

core spectrum are similarly reproduced in the crystal valence-band spectra, although their energy separation from the main line is somewhat reduced. In the valence spectra they now occur at ~1.6 and ~6 eV from the main line, with the additional complexity that the lowest-energy feature appears split. The filling of the large trough ~4.5 eV below the main line in the valence spectra relative to the core spectrum has been attributed to the presence of a broad oxygen $2p$ valence band at this energy in both early photoemission[31,5] and later theoretical works.[32] However, only the intensity of the O $2s$ level in the scaled spectra modulates with the placement of the x-ray standing-wave field; i.e., the line shapes of the two valence spectra recorded with the maximum of the electric-field intensity placed on either the Ni or O atomic sites are indistinguishable above the kinetic energy of the O $2s$ line. Consequently, it is clear that the filling of the trough ~4.5 eV below the Ni $3d$ main line in the valence versus core spectrum must be due to emission from Ni derived states, rather than from an O $2p$ band, which is counter to the previous interpretations.[31,5,32,2]

V. DISCUSSION

A. Covalent semiconductors

In order to critically evaluate our theory for valence x-ray standing-wave emission presented in Sec. II, we begin our discussion with crystalline Ge. For a homopolar material such as crystalline Ge that has two atoms in its primitive unit cell, the quantum mechanical parameters of Eq. (19) are identical for each of the two Ge atoms: $u_a = u_c = 1/\sqrt{2}$ and $\sigma_a^T = \sigma_c^T$. In our x-ray energy limit of two independent emitters, the valence-electron emission pattern should therefore appear similar to the core-level emission pattern recorded by monitoring the more tightly bound Ge $3d$ core electrons. As seen from Fig. 1, this is indeed the case.

The data from crystalline Ge therefore preclude any significant (>5%) electron emission emanating from the bonding-charge region between the cores. Had our data been sensitive to this region of intramolecular bonding charge, then the XSW-emission pattern from the valence electrons would dramatically differ from the XSW-emission pattern from the electronic cores. In fact, due to the large amount of bonding charge that is amassed between the atoms,[33] it was presumed by us that the amplitude of the valence-emission pattern would be reduced by a considerable fraction relative to the core-emission pattern. For example, F would be identically equal to zero for a uniform emission of electrons from throughout the unit-cell volume. Rather, our data have determined $D = 0.000 \pm 0.011$ and $F = 0.66 \pm 0.05$ for the valence distribution, which shows only a small reduction in XSW amplitude relative to the ideal core distribution.

In order to reconcile our physical intuition with the measurement, it is necessary to examine the basic physics of the photoemission process that leads to these emission patterns. For core states at typical x-ray energies, the product of $\mathbf{k}\cdot\mathbf{r}_e$ will be much less than 1 wherever the core-wave function gives an appreciable contribution to the matrix elements of the photoionization process. Consequently, the spatial part as well as the directions of propagation of the incident and

reflected photon beams of the electric field will not effect the integrals of Eq. (7). Hence, in the dipole approximation, the electron emission is found to be directly proportional to the electric-field intensities at the locations of the atomic cores.

Due to the large spatial extent of the valence wave functions, this situation will not hold for arbitrarily low photon energy; however, because the valence electrons have negligible binding energy ($\hbar^2 k_f^2/2m = \hbar\omega - \varepsilon_b$; $\varepsilon_b \sim 0$), the dipole approximation becomes a good approximation at the low x-ray energies as the final state quickly approaches an energetic plane wave ($e^{i\mathbf{k}_f\cdot\mathbf{r}}$; Born approximation). Because the transition probability is proportional to the overlap between the initial-and final-state wave functions, for this rapidly varying final state there will only be contributions to the photocurrent from the spatial regions where the initial state is also rapidly varying; i.e., the slowly varying regions will integrate to zero. As we know from the orthogonality relationship between the valence and core states in the region of the nucleus[34] and the resulting success of pseudopotential theory,[33] the initial valence states have appreciable high-frequency Fourier components only in the immediate vicinity of their electronic cores. Consequently, it is this effective localization of the valence emitter[35] for high-kinetic-energy final states that is responsible for the core-like behavior of the valence-XSW yield.

In early photoemission studies this phenomenon was illustrated schematically by matching the curvature of the initial-state wave function to the de Broglie wavelength of the ejected photoelectron;[36,27] only in the immediate vicinity of the electronic cores does a significant overlap between the initial and outgoing electron-wave functions exist. Additionally, because $k_f \gg k_{o,h}$ for valence states in our low x-ray energy range, the contribution to the emission pattern from the photon momentum is small ($<5\%$), and the resulting angular distribution may be considered dipole-like.[13]

From the angle integrated theory presented in Sec. II as well as the above analysis, it is clear that x-ray standing-wave measurements utilizing tightly bound core levels can only sense the spatial distribution of the atomic wave function through nondipole contributions to the photoyield. For valence emission, the interference term can also contribute to the yield from regions away from the cores because it contains nonlinear terms that depend on the electric-field intensity midway between the atoms [Eq. (16)]. Due to the high kinetic energy of the final-state electron, the contribution from these terms should be negligible compared to the localized core portion of the yield. Even for wave functions that are significantly delocalized due to the chemical bonding (Wannier functions), the magnitude of the interference terms should not be effected because they contain only the product of the anion and cation matrix elements, rather than a dependence on the actual overlap between the anion and cation wave functions. Consequently, the contribution from the interference term is not expected to increase as the atomic wave functions become delocalized, whereas the nondipole contributions to the photoelectron yield should increase because the product of $\mathbf{k}\cdot\mathbf{r}_e$ increases away from the cores. From comparison of the core- and valence-XSW emission patterns of crystalline Ge, it is evident that the quadrupole contribution Q to the valence-XSW yield is only a few percent,[37] which quantitatively accounts for the small observed reduction in coherent fraction (and hence the sensitivity to the spatial distribution of the valence wave function).

To explore the distortion of the atomic orbitals by the solid-state bonding, we may quantitatively examine the derived structural parameters from the heteropolar semiconductors and compare them to their atomic counterparts. As we have already argued that the basic form of Eq. (16) is not altered by the chemical bonding, deviations from atomic behavior should be reflected as observable differences in the fundamental parameters of our model.

For the case of heteropolar bond, the anions and cations have different atomic cross sections, and charge is transferred from the less electronegative cation to the more electronegative anion. As the positions of the anion and cation are known [$\mathbf{h}\cdot\mathbf{r}_a = -\pi/4$ and $\mathbf{h}\cdot\mathbf{r}_c = +\pi/4$ for the (111) reflections], we may use the x-ray standing-wave structure factor of Eq. (22) to derive an expression for the coherent positions and fractions for the valence-XSW distribution of the zincblende semiconductors. Due to the symmetry of the zinc blende structure, the $(-1-1-1)$ reflections will have the same coherent fractions as the (111) reflections, but the coherent positions will be of opposite sign. For the (111) reflection the result is

$$D = (2\pi)^{-1}\tan^{-1}\{[(1-\alpha_p)\sigma_c^T - (1+\alpha_p)\sigma_a^T] / [(1-\alpha_p)\sigma_c^T + (1+\alpha_p)\sigma_a^T]\} \tag{27}$$

and

$$F = [(1-\alpha_p)^2\sigma_c^{T^2} + (1+\alpha_p)^2\sigma_a^{T^2}]^{1/2}/[(1-\alpha_p)\sigma_c^T + (1+\alpha_p)\sigma_a^T]. \tag{28}$$

Table II lists the atomic cross sections of the valence electrons in Ga, As, In, and P calculated using the multiconfiguration Dirac-Fock method.[38] The calculations have been performed at 1900 eV photon energy for GaAs and 1830 eV photon energy for InP; i.e., close to the (111) Bragg back-reflection condition for each crystal. The calculations were performed for the ground state of each atom; i.e., Ga $4s^2 4p^1$, As $4s^2 4p^3$, In $5s^2 5p^1$, and P $3s^2 3p^3$. Consequently, each atomic cross section reflects the fractional occupancy of each atomic subshell. Also listed are the bond polarities from Ref. [11].

For our measurements of the scanned valence XSW emissions of the covalent semiconductors, we monitored the emission from the top of the crystal-valence bands. As these states are mostly of p character,[28] it is appropriate to compare our results to the theoretical values of D and F calculated from Eqs. (27) and (28) using the atomic cross sections and bond polarities α_p for p states; however, for comparison, we have also listed the bond polarities α_p^h and the resulting structural parameters assuming complete sp^3 hybridization across the entire valence band. The theoretical values of D and F are compared to the experimental values obtained from the fits in Table I. Here we have statistically combined the results for the (111) and $(-1-1-1)$ reflections to reduce

TABLE II. Theoretical atomic photoionization cross sections of the valence levels of GaAs at 1900 eV and of InP at 1830 eV photon energy (in barns). Note that the cross sections reflect the occupancy of each orbital. Also listed are the bond polarities α_p and α_P^h and the theoretical and experimental values for D and F.

GaAs				
		$4s$		$4p$
$Ga(4s^2 4p^1)$		661.5		107.9
$As(4s^2 4p^3)$		1197.5		752.6
α_p	0.47	α_p^h	0.32	
VB	Theory			
	$D=-0.100$		$F=0.88$	
VB^h	Theory			
	$D=-0.086$		$F=0.82$	
VB	Experiment			
	$D=-0.060\pm0.008$		$F=+0.648\pm0.033$	
Inp				
		$5s$		$5p$
$In(5s^2 5p^1)$		596.2		141.4
		$3s$		$3p$
$P(3s^2 3p^3)$		983.3		303.6
α_p	0.58	α_p^h	0.40	
VB	Theory			
	$D=-0.068$		$F=0.78$	
VB^h	Theory			
	$D=-0.066$		$F=0.77$	
VB	Experiment			
	$D=+0.056\pm0.009$		$F=+0.691\pm0.040$	

the experimental error. In each case, the experimental values for the (111) and $(-1-1-1)$ coherent positions for the two reflections are equal in magnitude, but of opposite sign within the experimental uncertainties as necessitated by symmetry. Due to the different roles of D and F in the XSW equation, our determination of the coherent fraction is not as accurate as our determination of the coherent position.

For both GaAs and InP, the theoretical description places the center of the valence-electron distribution much closer to the anion sites than what is experimentally observed. The fact that the two experimental distributions are shifted in opposite directions relative to the direction of electron-charge transfer; i.e., towards the anion sites for GaAs, but towards the cation sites for InP, clearly illustrates the importance of the photoionization cross sections in the analysis. The unsatisfactory comparison of theory with experiment most likely lies with the theoretical overestimate of the anion cross sections relative to the cation cross sections in going from the atomic to the solid state. Obviously, the solid-state bonding suppresses the emission from the anions relative to the cations. Such effects have been shown to influence the s-p cross-section ratio in the valence band of the elemental semiconductors[39] as well as the magnitude of the Cooper minimum in d-shell metals.[40]

This large discrepancy may most likely be traced to the covalent nature of the bonding within these crystals. As seen from the charge-density plots calculated by Chelikowsky and Cohen,[41] a large fraction of the valence charge associated with the anion resides in the bonding region between the cores. We have already demonstrated that charge density in this region is not visible to the x rays. Consequently, a large fraction of the charge that has been transferred from the anion to the cation will not contribute to the photoyield, leading to an effectively smaller experimental measure of either the effective charge transfer or its proximity to the anion sites.

The above formalism may be reversed to obtain the relative cross sections on a per electron basis (σ_a^T/σ_c^T) from the XSW measurements and the theoretical values of the bond polarities alone. For GaAs the ratio is 0.83, while for InP the ratio is 0.12. These ratios are much smaller than the theoretical predictions of 2.32 for GaAs and 0.72 for InP based on the theoretical calculations of the atomic cross sections; i.e., $(\sigma_a^T/\sigma_c^T)_{\text{solid}} \ll (\sigma_a^T/\sigma_c^T)_{\text{atomic}}$. The larger discrepancy in the case of InP versus GaAs may be attributed to the larger amount of charge that is transferred from the cation to the anion in the former case. Note that for a homopolar material like crystalline Ge, $(\sigma_a^T/\sigma_c^T)_{\text{solid}} = (\sigma_a^T/\sigma_c^T)_{\text{atomic}} = 1$, which is consistent with the above analysis.

B. Site-specific valence-electronic structure

Although quantitative agreement with the quantum mechanical parameters for the heteropolar semiconductors as calculated from the free-atom wave functions may be lacking, it remains clear that little emission emanates from the bonding region between the cores. Additionally, the Cu data has shown that the behavior of the valence-electron emission in the presence of the x-ray standing-wave interference field is independent of the binding energy of the particular electronic state near the core. Consequently, the emission probability of each energy state associated with the crystal-valence band must have the same approximate linear relationship with the electric-field intensity at its core site.

These considerations lead to the following energy-dependent generalization of Eq. (19) for the valence photocurrent $(C=1)$ in the dipole approximation

$$I(E,\hbar\omega) \propto \sum_i \rho_i(E)\sigma_i(E,\hbar\omega)[1+R+2\sqrt{R}\cos(\nu+\mathbf{h}\cdot\mathbf{r}_i)]. \tag{29}$$

Here the $\rho_i(E)$ are the partial density of states. We have written them in place of the energy-dependent bond polarities $u_i^2(E)$ that may be interpreted as the probability of finding an electron with binding energy E on the ith atom of the crystalline-unit cell. The $\sigma_i(E,\hbar\omega)$ are the energy-dependent photoionization cross sections. They include both binding-energy and photon-energy dependence to account for the different angular-momentum[42] and energy states of the crystal-valence band as well as for the shrinking of the valence emitter with increasing photon energy;[35] i.e., the spatial dependences of the initial-state wave functions. Both the $\rho_i(E)$ and the $\sigma_i(E,\hbar\omega)$ extend over the entire energy width of the crystal-valence band. Note that Eq. (29) reduces to the com-

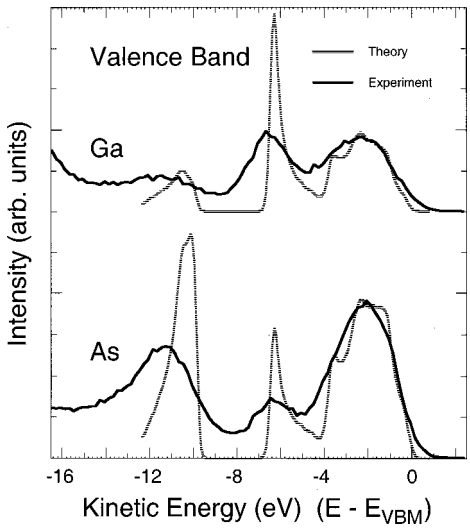

FIG. 13. Comparison of the *chemically resolved* Ga and As contributions to the GaAs valence band with the theoretically calculated Ga and As partial density of states. The upper portion of the figure shows the cation contributions, and the lower portion of the figure shows the anion contributions. The spectra have been offset for clarity. The solid lines are the experimental data, and the shaded lines are the theoretical calculations.

monly used expression for the valence photocurrent when $R=0$; i.e., in the presence of only one monochromatic photon beam[4,6]

$$I(E,\hbar\omega)\alpha\sum_i \rho_i(E)\sigma_i(E,\hbar\omega). \tag{30}$$

From Eq. (29) it is clear that the individual chemical components of a crystal-valence band may be obtained from valence-photoelectron spectra recorded at different electric-field conditions around the Bragg reflection by solving a simple set of linear equations. The coefficients of the individual components to the valence spectra are the relative electric-field intensities at the different atomic sites; they may be either calculated theoretically, as in Fig. 7, or determined experimentally from core-level data.

Figure 13 shows the resulting chemically resolved components of the GaAs valence band obtained by taking the appropriate linear combinations of the spectra from Fig. 8. Indeed, the difference between the Ga- and As-related curves is greatly enhanced with respect to Fig. 8. These components are compared to an *ab initio* theoretical calculation of the Ga and As partial density of states computed by Chelikowsky's group by using *ab initio* pseudopotentials within density functional theory with a plane-wave basis.[43,28] The site-specific density of states curves were computed by using a sphere corresponding to the Ga-As covalent radius centered on each atom to deconvolute the obtained wave functions over atomic orbitals of valence electrons.

The calculation clearly shows the differences between the two electronic structures centered around each atomic core. These differences occur due to the natural ordering of the Ga and As atomic $4s$ and $4p$ valence states, coupled with the solid-state bonding that has occurred between them. Remarkable qualitative agreement between theory and experiment is observed, even though experimental resolution and cross-section effects have not been considered theoretically.

C. Cu

The Cu data experimentally confirm that the entire energy spectrum of the crystal-valence band has the same, approximate linear response to the x-ray standing-wave field intensity at the position of its atomic cores, regardless of the particular initial-state binding energy or valence wave function. This result has provided the experimental basis for our linear decomposition of the valence band into its individual, site specific components; it is equivalent to saying that the quadrupole contribution Q is equivalent for each energy state of the valence band, within our experimental resolution. In addition to providing this important piece of experimental evidence, the Cu data also give unique experimental confirmation of an important theoretical premise that has been used in band-structure calculations for over 6 decades.

In 1940, Herring[34] noted that because both the valence states and the core states of a crystal are solutions to the crystal Schrodinger equation, the valence states must be orthogonal to the core states in the spatial region of the cores because the core states vanish outside the region of the nucleus. Additionally, the valence wave functions of the crystal must resemble the atomic wave functions of the individual atoms in the region of the cores because the core wave functions are not significantly altered by the atomic bonding. We have already used this result in our earlier discussion of the x-ray standing-wave valence-structure factor. Furthermore, because the nuclear potential is weak between the cores, the valence wave functions there should be nearly free-electron or plane-wave-like. Consequently, Herring conjectured that only a few plane waves that have been orthogonalized to the core states would be needed to represent the entire eigenfunction spectrum of the crystal potential[33]

$$\psi(\mathbf{r})=\sum_k a_k \ \mathrm{OPW}_k, \tag{31}$$

where

$$\mathrm{OPW}_k=|\mathbf{k}\rangle-\textstyle\sum_{t,j}|t,j\rangle\langle t,j|\mathbf{k}\rangle. \tag{32}$$

Here $|\mathbf{k}\rangle=V^{1/2}e^{i\mathbf{k}\cdot\mathbf{r}}$ are the normalized, plane-wave parts of the valence-wave function that extend throughout the crystal, and $|t,j\rangle=\phi_t(\mathbf{r}-\mathbf{r}_j)$ are the normalized, t core eigenstates that are centered at the individual ion positions j.

In the x-ray limit, only the rapidly oscillating core parts of Eq. (31) will contribute to the matrix elements of Eq. (17) because $a_k\rightarrow 0$ as $k\rightarrow\infty$ and k_f is very large. This situation provides little final-state overlap with the more slowly varying plane-wave parts of the initial-state eigenfunctions. Consequently, the x-ray valence photocurrent will consist of a significant core part plus a much smaller and inconsequential plane-wave part, as is evidenced even for the most loosely bound valence states residing at the Fermi level. The fact that

all energy states of the valence band have the same approximate linear response to the electric-field intensity is apparently also a consequence of Herring's principles; i.e., that in the region near the nucleus, the solutions of the wave equation do not depend very much on the energy of the state because the negative potential of the nucleus is so large.[34]

D. NiO

Although one of the first photoemission studies of NiO was published in 1973,[31] the NiO photoemission spectra have continued to receive considerable theoretical and experimental attention. The reason for the ambiguities that have persisted may be attributed to the large contributions of many-body effects to both the initial- and final-state wave functions. Although the photoemission process is a many-body phenomenon in general, for the simple semiconductors and metals, a one-electron picture adequately describes the features which we have already discussed. However, in the case of the transition-metal oxides such as NiO, strong electron correlations between the valence d electrons make interpretations of the different photoemission spectra in such single-particle approximations impossible. Additionally, it is recognized that NiO is a charge-transfer insulator, so electronic excitations from the ligand $2p$ orbitals to the unfilled metal $3d$ shell are commonly observed in both x-ray absorption and electron-emission experiments.

One of the first theoretical calculations of the NiO valence-photoemission spectrum was presented by Fujimori *et al.*[32] In their work they utilized a configuration-interaction wave function for an octahedral metal-ligand $[NiO_6]^{-10}$ cluster that took into account the different charge-transfer configurations of the initial ground state:

$$\psi_g = \alpha|d^8\rangle + \beta|d^9\underline{L}^1\rangle. \tag{33}$$

Here d^8 represents the $3d$ valence electrons of the Ni^{+2} ion, and $\underline{L}$ represents a hole in an O^{-2} ligand-bonding orbital that has transferred an electron to the Ni ion. The second term in Eq. (33) therefore corresponds to the finite probability of finding an O ligand electron on a Ni site. Consequently, a valence photoionization event produces the following mixture of final ionization states:

$$\psi_f = \alpha'|d^7\rangle + \beta'|d^8\underline{L}^1\rangle + \beta''|d^9\underline{L}^2\rangle. \tag{34}$$

To complicate this configuration-interaction wave function further, both the initial and final states of the Ni $3d$ electrons are split by the crystal-field potential, as well as by the Coulomb and exchange interactions of the remaining holes. Despite the complexity of this analysis, the calculated valence-photoemission spectra were found to agree remarkably well with the experimental data. The primary result was that the main line lying closest to the Fermi energy was found not to be due to a d^7 final state as had been originally interpreted,[31] but rather to a d^8 final state that was produced by a ligand to metal electron-charge transfer; i.e., a final state with considerable $|d^8\underline{L}^1\rangle$ character.

One necessity, however, for the agreement of the calculation with the experimental data was the inclusion of a wide O $2p$ band lying approximately 4 eV below the valence-band maximum. Previous evidence for the existence of this band was provided by experimental valence-band photoemission studies of other transition-metal oxides,[31] such as TiO_2, that were believed to have nonoverlapping metal $3d$ and O $2p$ states.[31,2] Additionally, analysis of the NiO valence spectra recorded at lower photon energies suggested large contributions from the O $2p$ band in this region as well.[5]

One of the more detailed resonant photoemission studies of NiO has been published by Tjernberg *et al.*[44] By examining the resonant behavior of the NiO valence band in the photon-energy range around the Ni $3p$ and Ni $2p$ core-photoionization thresholds, these authors were able to confirm the existence of the localized Ni $3d$ states predicted by theory. However, these authors found no resonances around the O $1s$ absorption threshold, which demonstrates either that the valence spectrum at these energies contains no strong oxygen emission or that the oxygen states are highly delocalized. An interesting observation from these data was that a peak ~4 eV below the valence-band maximum previously attributed to O $2p$ emission in the earlier resonant-photoemission study by Oh *et al.*[45] was found to resonate strongly at the Ni $3p$ absorption edge which supports the assignment of this feature to the Ni density of states. Additionally, strong emission from Ni states within the energy range of the O $2p$ level is observed in the theoretical valence-band study of van Elp *et al.*[46] as well as in modified local-density approximation calculations[47] and angle-resolved photoemission studies.[48]

As we have already concluded, the contribution from the O $2p$ states to the valence-band spectra must be negligible, because the O $2s$ level shows strong modulation with the placement of the XSW-field intensity in the scaled spectra that the higher kinetic-energy region does not. The fact that there are negligible lineshape changes in the energy region of the $3d$ emission demonstrates that the O $2p$ band does not give any significant contribution to the valence photocurrent at these photon energies. Our estimate of the emission intensity from the O $2p$ band relative to the Ni $3d$ band is about 1/40, compared to a peak-to-peak height of roughly 1/5 in the spectra calculated by Fujimori *et al.*[32] and even larger contributions in the atomic cross-section deconvolutions of the experimental data.[5] Consequently, we must conclude that the Ni valence band in NiO is wider than the simple crystal-field and atomic-multiplet theories of a $[NiO_6]^{-10}$ cluster predict.

VI. CONCLUSIONS

In conclusion, we have examined the behavior of the valence-photoelectron emission from a series of crystals that span the entire range of solid-state bonding under the condition of strong x-ray Bragg reflection. We find that the valence-electron emission arises from a region close to the atomic cores in our x-ray energy range, even for electron states lying close to a metallic Fermi edge. We have explained this finding by examining the basic physics of the photoemission process. Additionally, we have derived a theoretical expression in terms of the bond polarities and valence-photoionization cross sections for the x-ray

standing-wave structure factor for valence-electron emission. Comparison of our data for the heteropolar semiconductors with the resulting theoretical structural parameters has revealed interesting solid-state contributions to the valence-photoionization cross sections. Furthermore, we have demonstrated that valence-photoelectron spectra recorded in the vicinity of a crystal x-ray Bragg reflection can reveal site specific valence information that is directly related to the partial density of occupied valence states. Our delineation of the GaAs valence band is in agreement with theory, and examination of the NiO valence band by the same technique reveals that little O $2p$ emission contributes to the valence photocurrent.

ACKNOWLEDGMENTS

The authors thank Dr. Mau Chen, Dr. Leeor Kronik, Dr. Michael Weinert, Dr. Jorg Zegenhagen, and Dr. Manuel Cardona for useful discussions. E. J. N. thanks the National Research Council for support. D. H. and J. W. acknowledge the Donors of the Petroleum Research Fund, administered by the American Chemical Society, for partial support of this research. This work was performed at the Stanford Synchrotron Radiation Laboratory which is supported by the United States Department of Energy, Office of Basic Energy Sciences, and at the National Synchrotron Light Source which is supported by the U.S. Department of Energy.

[1] A. Einstein, Ann. Phys. (N.Y.) **17**, 132 (1905); **20**, 199 (1906).

[2] See for example, *Photoemission in Solids I*, edited by M. Cardona and L. Ley, Topics in Applied Physics No. 26 (Springer-Verlag, Berlin, 1978); *Photoemission in Solids II*, edited by M. Cardona and L. Ley, Topics in Applied Physics No. 27 (Springer-Verlag, Berlin, 1978); *Photoelectron Spectroscopy: Principles and Applications*, 2nd ed., edited by S. Hufner (Springer-Verlag, Berlin, 1996).

[3] J. W. Cooper, Phys. Rev. **128**, 681 (1962).

[4] W. Braun, A. Goldmann, and M. Cardona, Phys. Rev. B **10**, 5069 (1974).

[5] D. E. Eastman and J. L. Freeouf, Phys. Rev. Lett. **34**, 395 (1975).

[6] T.-U. Nahm, M. Han, S.-J. Oh, J.-H. Park, J. W. Allen, and S.-M. Chung, Phys. Rev. Lett. **70**, 3663 (1993); T.-U. Nahm, M. Han, S.-J. Oh, J.-H. Park, J. W. Allen, and S.-M. Chung, Phys. Rev. B **51**, 8140 (1995); T.-U. Nahm, R. Jung, J.-Y. Kim, W.-G. Park, S.-J. Oh, J.-H. Park, J. W. Allen, S.-M. Chung, Y. S. Lee, and C. N. Whang, *ibid.* **58**, 9817 (1998).

[7] U. Fano, Phys. Rev. **124**, 1866 (1961).

[8] L. Ley, M. Taniguchi, J. Ghijsen, R. L. Johnson, and A. Fujimori, Phys. Rev. B **35**, 2839 (1987); D. Brown, M. D. Crapper, K. H. Bedwell, M. T. Butterfield, S. J. Guilfoyle, A. E. R. Malins, and M. Petty, *ibid.* **57**, 1563 (1998); J. Okabayashi, A. Kimura, T. Mizokawa, A. Fujimori, T. Hayashi, and M. Tanaka, *ibid.* **59**, 2486 (1999).

[9] A. Stuck, J. Osterwalder, T. Greber, S. Hufner, and L. Schlapbach, Phys. Rev. Lett. **65**, 3029 (1990).

[10] D. P. Woodruff, D. L. Seymour, C. F. McConville, C. E. Riley, M. D. Crapper, N. P. Prince, and R. G. Jones, Surf. Sci. **195**, 237 (1988); J. Zegenhagen, Surf. Sci. Rep. **18**, 199 (1993).

[11] W. A. Harrison, *Electronic Structure and the Properties of Solids* (Freeman, San Francisco, 1980), Chaps. 3 and 7.

[12] N. W. Ashcroft and N. D. Mermin, *Solid State Physics* (Holt, Rinehart and Winston, New York, 1976), Chap. 10, Appendix F.

[13] H. A. Bethe and E. E. Salpeter, *Quantum Mechanics of One- and Two-Electron Atoms* (Plenum, New York, 1977), Chap. 4.

[14] B. W. Batterman and H. Cole, Rev. Mod. Phys. **36**, 681 (1964).

[15] V. G. Aleshin and Yu. N. Kucherenko, J. Electron Spectrosc. Relat. Phenom. **8**, 411 (1976).

[16] A. L. Fetter and J. D. Walecka, *Theoretical Mechanics of Particles and Continua* (McGraw-Hill, New York, 1980), Chap. 10.

[17] E. Fontes, J. R. Patel, and F. Comin, Phys. Rev. Lett. **70**, 2790 (1993).

[18] I. A. Vartanyants and J. Zegenhagen, Solid State Commun. **113**, 299 (1999).

[19] J. R. Patel, D. W. Berreman, F. Sette, P. H. Citrin, J. E. Rowe, P. L. Cowan, T. Jach, and B. A. Karlin, Phys. Rev. B **40**, 1330 (1989).

[20] J. C. Woicik, T. Kendelewicz, K. E. Miyano, P. L. Cowan, C. E. Bouldin, B. A. Karlin, P. Pianetta, and W. E. Spicer, Phys. Rev. Lett. **68**, 341 (1992); T. Kendelewicz, J. C. Woicik, K. E. Miyano, A. Herrera-Gomez, P. L. Cowan, B. A. Karlin, C. E. Bouldin, P. Pianetta, and W. E. Spicer, Phys. Rev. B **46**, R7276 (1992); J. C. Woicik, T. Kendelewicz, A. H. Gomez, K. E. Miyano, P. L. Cowan, C. E. Bouldin, P. Pianetta, and W. E. Spicer, Phys. Rev. Lett. **71**, 1204 (1993).

[21] J. C. Woicik, E. J. Nelson, and P. Pianetta, Phys. Rev. Lett. **84**, 773 (2000).

[22] H. Kuhlenbeck, G. Odorfer, R. Jaeger, G. Illing, M. Menges, Th. Mull, H.-J. Freund, M. Pohlchen, V. Staemmler, S. Witzel, C. Scharfschwerdt, K. Wennemann, T. Liedtke, and M. Neumann, Phys. Rev. B **43**, 1969 (1991); M. Baumer, D. Cappus, G. Illing, H. Kuhlenbeck, and H.-J. Freund, J. Vac. Sci. Technol. A **10**, 2407 (1992); St. Uhlenbrock, C. Scharfschwerdt, M. Neumann, G. Illing, and H.-J. Freund, J. Phys.: Condens. Matter **4**, 7973 (1992).

[23] J. R. Patel and J. A. Golovchenko, Phys. Rev. Lett. **50**, 1858 (1983).

[24] Error bars reflect the spread of values that double the residual chi-squared error.

[25] The inclusion of the Debye-Waller factor would reduce the ideal, bulk coherent fraction from 0.71 to 0.69.

[26] M. J. Bedzyk, G. Materlik, and M. V. Kovalchuk, Phys. Rev. B **30**, 2453 (1984); M. J. Bedzyk and G. Materlik, *ibid.* **32**, 6456 (1985).

[27] L. Ley, R. A. Pollak, F. R. McFeely, S. P. Kowalczyk, and D. A. Shirley, Phys. Rev. B **9**, 600 (1974).

[28] M. L. Cohen and J. R. Chelikowsky, *Electronic Structure and Optical Properties of Semiconductors*, Springer Series in Solid-State Sciences No. 75 (Springer-Verlag, Berlin, 1988), Chap. 6.

[29] G. A. Burdick, Phys. Rev. **129**, 138 (1963).

[30] C. Kittel, *Introduction to Solid State Physics* (Wiley, New York, 1976), 5th ed., Chap. 1.

[31] S. Hufner and G. K. Wertheim, Phys. Rev. B **8**, 4857 (1973).
[32] A. Fujimori, F. Minami, and S. Sugano, Phys. Rev. B **29**, 5225 (1984); A. Fujimori and F. Minami, *ibid.* **30**, 957 (1984).
[33] W. A. Harrison, *Solid State Theory* (Dover, New York, 1979), Chaps. 1 and 2.
[34] C. Herring, Phys. Rev. **57**, 1169 (1940).
[35] C. Solterbeck, W. Schattke, J.-W. Zahlmann-Nowitzki, K.-U. Gawlik, L. Kipp, M. Skibowski, C. S. Fadley, and M. A. Van Hove, Phys. Rev. Lett. **79**, 4681 (1997).
[36] W. C. Price, A. W. Potts, and D. G. Streets, in *Electron Spectroscopy*, edited by D. A. Shirley (North-Holland, Amsterdam, 1972).
[37] H. Wagenfeld, Phys. Rev. **144**, 216 (1966).
[38] The atomic cross-section calculations were performed by Dr. Mau H. Chen of Lawrence Livermore National Laboratory.
[39] R. G. Cavell, S. P. Kowalcyk, L. Ley, R. A. Pollak, B. Mills, D. A. Shirley, and W. Perry, Phys. Rev. B **7**, 5313 (1973).
[40] I. Abbati, L. Braicovich, G. Rossi, I. Lindau, U. del Pennino, and S. Nannarone, Phys. Rev. Lett. **50**, 1799 (1983); G. Rossi, I. Lindau, L. Braicovich, and I. Abbati, Phys. Rev. B **28**, 3031 (1983).
[41] J. R. Chelikowsky and M. L. Cohen, Phys. Rev. B **14**, 556 (1976).
[42] In general, this sum should include the individual angular-momentum components of the density of states;[6] however, for simplicity we have written $\rho_i(E)\sigma_i(E,\hbar\omega)=\Sigma_j\rho_{i,j}(E)\sigma_{i,j}\times(E,\hbar\omega)$, where j is the angular momentum.
[43] J. C. Woicik, E. J. Nelson, T. Kendelewicz, P. Pianetta, M. Jain, L. Kronik, and J. R. Chelikowsky, Phys. Rev. B **63**, R041403 (2001).
[44] O. Tjernberg, S. Soderholm, U. O. Karlsson, G. Chiaia, M. Qvarford, H. Nylen, and I. Lindau, Phys. Rev. B **53**, 10 372 (1996).
[45] S. J. Oh, J. W. Allen, I. Lindau, and J. C. Mikkelsen, Jr., Phys. Rev. B **26**, 4845 (1982).
[46] J. van Elp, H. Eskes, P. Kuiper, and G. A. Sawatzky, Phys. Rev. B **45**, 1612 (1992).
[47] V. I. Anisimov, I. V. Solovyev, M. A. Korotin, M. T. Czyzyk, and G. A. Sawatzky, Phys. Rev. B **48**, 16 929 (1993).
[48] Z.-X. Shen, C. K. Shih, O. Jepsen, W. E. Spicer, I. Lindau, and J. W. Allen, Phys. Rev. Lett. **64**, 2442 (1990); Z.-X. Shen, R. S. List, D. S. Dessau, B. O. Wells, O. Jepsen, A. J. Arko, R. Barttlet, C. K. Shih, F. Parmigiani, J. C. Huang, and P. A. P. Lindberg, Phys. Rev. B **44**, 3604 (1991).